Research Square

Preprints are preliminary reports that have not undergone peer review.
They should not be considered conclusive, used to inform clinical practice,
or referenced by the media as validated information.

Radiation-induced Tuning of Magnetoelectric and Cryogenic Transport Properties in Zro2 -doped Bi0.85sb0.15 SOLID Solutions

Bayram Mehdiyev
Azerbaijan University of Architecture and Construction
Ilaha Abdullayeva
ilahe.abdullayeva1909@gmail.com

Azerbaijan University of Architecture and Construction

Research Article

Keywords: Bismuth-antimony alloys, Cryogenic transport, Gamma irradiation, Radiation defects, Carrier mobility, Magnetoelectric properties, Extrusion

Posted Date: August 31st, 2026

DOI: https://doi.org/10.21203/rs.3.rs-10744341/v1

License: This work is licensed under a Creative Commons Attribution 4.0 International License.
Read Full License

Additional Declarations: No competing interests reported.

Abstract

This study investigates the temperature-dependent (77–300 K) electrical and thermal transport properties of ZrO_2-modified $Bi_{0.85}Sb_{0.15}$<Te> extruded alloys subjected to gamma-ray irradiation under an applied magnetic field of 740 kA/m. The results reveal that low-dose gamma irradiation significantly enhances charge carrier mobility. This enhancement is predominantly driven by the radiation-induced generation of acceptor-type (negatively charged) defects and the partial neutralization of intrinsic scattering centers, which effectively suppresses impurity scattering efficiency. Furthermore, gamma quanta exposure induces a continuous structural rearrangement of point defects within the extruded $Bi_{0.85}Sb_{0.15}$<Te> matrix. This dynamic process alters the localized state spectrum and modifies electron scattering mechanisms, directly influencing the thermoelectric and magnetoelectric performance of the composite across cryogenic temperatures. These findings provide critical insights into tailoring the low-temperature transport behavior of bismuth-antimony solid solutions via combined nanoparticle modification and radiation engineering.

1. Introduction

Single crystals and highly texturized extruded alloys based on the Bismuth–Antimony (Bi-Sb) solid solution system are well-established key materials for low-temperature energy conversion and cryogenic solid-state cooling applications [1–8]. Owing to their small energy bandgap, high carrier mobility, and pronounced anisotropic transport properties at temperatures below 150 K, these systems serve as core components in radiation thermoelements and optical sensors deployed for measuring high-power thermal fluxes and laser emissions [9, 10]. However, the modern operational environments of space exploration, nuclear power engineering, and high-energy physics demand electronic devices capable of maintaining performance under intense exposure to ionizing radiation [11, 12]. The conversion efficiency of a thermoelectric material is characterized by the dimensionless figure of merit, $Z = \alpha^2\sigma/\chi$, is the Seebeck coefficient, σ is the electrical conductivity, and χ is the total thermal conductivity (composed of electronic χ_e and lattice χ_l contributions). Elevating Z requires an optimal trade-off: decoupling electrical and thermal transport by scattering heat-carrying acoustic phonons more effectively than electrical charge carriers [13, 14]. A widely adopted technique to achieve this involves introducing nano-scale elastic strain fields or secondary phase dispersoids into the matrix [15, 16]. Specifically, modifying the Bi-Sb semiconductor matrix with fine oxide particles such as Zirconium Dioxide (ZrO_2) introduces localized internal stresses due to the mismatch in the Coefficient of Thermal Expansion (CTE) between the matrix and the dispersoid. These stress fields act as selective scattering centers, reducing lattice thermal conductivity χ_l with minimal degradation to carrier conductivity [17, 18].

Concurrently, exposure to ionizing radiation alters the defect structure of semiconductors by generating primary radiation defects and induced defect complexes [19, 20]. While radiation-induced defect formation can adversely degrade device performance, controlled gamma irradiation offers a tool for engineering defect states, tailoring charge carrier concentrations, and modifying scattering mechanisms

[21, 22]. Despite extensive studies on conventional Bi-Sb alloys, the synergistic influence of ZrO_2 particle modification, tellurium (Te) donor doping, and gamma-quanta irradiation on the magnetoelectric and cryogenic transport properties of extruded Bi-Sb solid solutions remains largely unexplored in literature [23, 24].

To address this gap, this study systematically investigates the temperature-dependent (77–300 K) and magnetic field-dependent (up to 740 kA/m) electrical, thermal, and magnetoelectric parameters of Te-doped, ZrO_2-modified $Bi_{0.85}Sb_{0.15}$ extruded alloys. The evolution of transport behavior is critically analyzed across pristine and gamma-irradiated states at doses of 1 Mrad, 10 Mrad, and 50 Mrad, focusing on the underlying defect generation, rearrangement, and carrier scattering mechanisms.

2. Experimental Details

2.1. Material Synthesis and Extrusion Process

High-purity elemental bismuth ("VI-0000", 99.9999\%), antimony ("SU-0000", 99.9999\%), and twice-sublimated tellurium (T-SCh grade) were utilized as starting components. The elemental precursors were weighed with an analytical accuracy of ± 0.0001g according to the stoichiometric ratio for the $Bi_{0.85}Sb_{0.15}$ solid solution. To achieve a tellurium dopant concentration of 0.0001 at% Te, a master alloy of $Bi_{0.85}Sb_{0.15}$ <0.1 at % Te > was synthesized first and subsequently diluted by direct fusion with stoichiometric, undoped $Bi_{0.85}Sb_{0.15}$. The synthesis was carried out in quartz ampoules previously etched in a chromic acid mixture ($K_2Cr_2O_7$+ H_2SO_4) and thoroughly rinsed with deionized water. The ampoules were evacuated to a residual pressure of ~ 10^{-2} Pa and sealed. Synthesis was executed at 673 K for 2 h with continuous mechanical agitation to ensure chemical homogeneity. Upon completion, the ampoules were rapidly quenched in room-temperature water.

The synthesized ingot was mechanically ground in a porcelain mortar to obtain a powder fraction with particle sizes ≤0.5 mm. Plasmachemically synthesized ZrO_2 nanoparticles (average grain diameter ~50 nm, melting point ~2950 K) were introduced as a modifying phase at a concentration of 1 wt %. The composite mixture was thoroughly homogenized and cold-pressed into cylindrical briquettes (Ø ~ 30 mm) under a compaction pressure of ~3.5 t/cm^2 (~ 343 MPa).

To optimize modifier dispersion within the matrix, the briquettes were subject to sub-melting annealing within the liquidus-solidus temperature window, where the liquid phase comprised 70–80 vol%. Hot extrusion was subsequently performed on an MS-1000 hydraulic press under superplastic deformation conditions without inducing macro- or micro-structural damage. The extrusion technological parameters were strictly controlled: extrusion temperature T_{ex} = 475 ±3K, extrusion pressure P_{ex} = 480 MPa, ram velocity v_{pr} = 0.02 cm/min, and drawing ratio λ = 25.

Following extrusion, the resulting rods were stress-relieved by annealing at 503 K for a specified duration in quartz ampoules evacuated to 10^{-2}Pa. Mechanical testing revealed that the flexural strength of the

extruded $Bi_{0.85}Sb_{0.15}$<Te> - ZrO_2 alloys was approximately 3 times higher than that of single crystals of identical chemical composition [25].

2.2. Structural Characterization and Radiation Exposure

Phase composition and preferred crystallographic orientation (texture) were investigated by X-ray Diffraction (XRD) using Bruker D8 ADVANCE and D2 PHASER diffractometers equipped with Cu-K_α radiation [26]. Rietveld refinement and phase verification performed via TOPAS-4.2 software confirmed that the composite powders crystallize in the rhombohedral system (space group $R\bar{3}m$, indexed in the hexagonal setting). Surface morphology and microstructural features were examined via Atomic Force Microscopy (AFM) on metallographic thin sections prepared using diamond polishing pastes.

For radiation damage studies, annealed specimens were irradiated with gamma-quanta from a ^{60}Co isotopic source at absorbed radiation doses of 1Mrad, 10 Mrad, and 50 Mrad (10 kGy, 100 kGy, and 500 kGy, respectively). The absorbed doses were calibrated by comparing electron densities with standard chemical dosimetric systems [27].

2.3. Low-Temperature Transport Property Measurements

Rectangular prism specimens with dimensions of 0.2 × 0.4 ×1.5 cm^3 were cut along the rod extrusion direction using electric spark machining. To remove the damaged, contaminated surface layer resulting from electro-discharge processing, samples underwent electrochemical etching in a KOH + $C_4H_6O_6$ + H_2O solution at ~300 K for 20–25 s at a current density of 0.5 A/cm^2 [28].

Low-temperature electric and thermal contacts (0.5 mm point contact diameter) were applied using Wood's alloy (25 wt% Bi + 50 wt% Pb + 12.5 wt% Sn + 12.5 wt% Cd, melting point ~343 K) with FSKGL active flux (CH_5ON_3 + HCl + $C_3H_8O_3$). Electrical conductivity (σ), Seebeck coefficient (α), Hall coefficient R_H), and total thermal conductivity (λ) were simultaneously measured along the extrusion axis in the temperature interval of 77–300 K under static magnetic fields up to H = 740 kA/m [29].

Voltages, thermoelectromotive forces (thermo-emf), and currents were recorded using high-precision digital voltmeters and ammeters (B7-21 and SM3D). Sample geometry and probe spacing were measured using an MBS-1 optical microscope with an accuracy class of ±0.005 mm. The calculated experimental uncertainties were within ± 3% for electrical transport parameters (σ, α, R_H) and ±5% for thermal conductivity (λ) [30].

3. Results and Discussion

3.1. Microstructural and Crystallographic Evolution Under Irradiation

The structural and crystallographic modifications induced by ZrO_2 incorporation and gamma irradiation were verified through X-ray diffraction (XRD) spectral refinement using TOPAS-4.2 and EVA software suites. The unit cell parameters and calculated crystallite sizes for pristine and irradiated $Bi_{0.85}Sb_{0.15}$<Te> - ZrO_2 extruded alloys are summarized in Table 1.

The XRD patterns reveal that increasing the gamma quanta dose leads to a progressive reduction in crystallite size, reflecting a radiation-induced degradation of crystalline perfection. This structural alteration is most pronounced in the 4th diffraction peak, which displays a systematic reduction in peak intensity accompanied by line broadening. Conversely, the unit cell lattice parameters remain practically unchanged across all radiation doses (Fig. 1 and Table 1), indicating that structural alterations are predominantly confined to point defect dynamics and micro-strain distribution rather than fundamental lattice expansion or contraction.

Table 1
Unit cell parameters and sizes of $Bi_{0.85}Sb_{0.15}$Te crystallites modified with ZrO_2

Dose	a	c	Gro.sp.	Size. crystallites, nm
1 - un irradiat.	4.5076	11.778	R3	96
2 - 1 Mrad	4.5104	11.780	R3	88
3 - 10 Mrad	4.5078	11.781	R3	81
4 - 50 Mrad	4.5125	11.788	R3	65

During the extrusion process, severe plastic deformation induces texture formation, orienting a high fraction of polycrystalline grains such that their trigonal axis aligns parallel to the extrusion axis [6, 31]. Structural defects resulting from this deformation are primarily localized between the basal cleavage planes (111). The addition of 1 wt% ZrO_2 particles significantly improves the microscopic spatial uniformity of dislocation distribution by providing pinning centers ("stoppers") that restrict dislocation movement.

The modifier geometry plays a key role: coarse particles block basal dislocation glide, small spherical nanoparticles activate pyramidal slip while partially suppressing basal slip, and pyramidal dispersoids promote multiple slip systems. Thermal stresses stemming from the CTE mismatch between the ZrO_2 nanoparticles and the $Bi_{0.85}Sb_{0.15}$ matrix further influence recrystallization kinetics and grain boundary mobility, thereby enhancing overall texture stability and mechanical strength.

The data obtained using X-ray phase analysis were also confirmed by AFM.

To gain deeper insights into the surface modification, defect dynamics, and microstructural evolution driven by gamma-quanta irradiation, three-dimensional (3D) Atomic Force Microscopy (AFM) analysis was conducted on the metallographic sections of Te-doped, ZrO_2-modified $Bi_{0.85}Sb_{0.15}$ extruded

composite alloys. The corresponding topographies for the pristine (unirradiated) and irradiated samples (1 Mrad, 10 Mrad and 50 Mrad) are depicted in Fig. 2a–d.

- Pristine State (Fig. 2a): The non-irradiated sample displays a macroscopically smooth, continuous matrix texture characteristic of highly oriented, plastically deformed extruded Bi - Sb alloys. The ZrO_2 nanoparticles (introduced at 1 wt%) act as dislocation stoppers during hot extrusion, resulting in a spatially uniform strain distribution without micro-cracks or severe local topographic fluctuations. The Z-axis relief indicates a relatively low surface roughness, dominated by the underlying texture parallel to the extrusion axis.
- Low Radiation Dose (1 Mrad, Fig. 2b): At an absorbed dose of 1Mrad, a subtle rearrangement of the surface micro-relief is observed. Low-dose gamma irradiation primarily induces the generation of primary point defects (vacancies and interstitials) alongside the partial annihilation of non-equilibrium deformation-induced structural defects. These point defects migrate toward localized stress sinks created by ZrO_2 nanoparticles and internal grain boundaries, facilitating local micro-stress relaxation. This structural redistribution manifests as a minor smoothing of fine surface asperities, which correlates directly with the observed enhancement in charge carrier mobility (μ_H) due to suppressed defect scattering.

- Intermediate Radiation Dose (10 Mrad, Fig. 2c): Upon increasing the radiation dose to 10 Mrad, a distinct morphological transition takes place. The surface topography exhibits regularized, directional step-like (ridge) structures along specific crystallographic planes (predominantly the basal cleavage (111) planes). This step formation is driven by the radiation-stimulated accumulation and condensation of vacancies and interstitial complexes into dislocation loops and planar defect walls. The interaction of these radiation-induced defect clusters with the internal elastic stress fields surrounding ZrO_2 dispersoids promotes localized crystallite rotation and dynamic substructural ordering.
- High Radiation Dose (50 Mrad, Fig. 2d): At the maximum dose of 50 Mrad, the 3D surface topography reveals severe structural fragmentation, heightened local surface roughness (R_q), and pronounced peak-to-valley variations along the Z-axis. Continuous exposure to high-energy gamma quanta causes high-density point defect saturation, leading to defect clustering, localized micro-strain buildup, and the partial breakdown of grain boundary coherence. This observed microstructural fragmentation accounts for the XRD peak intensity attenuation and line broadening described earlier, as well as the observed decrease in electrical conductivity (σ) due to intensified carrier scattering at high-density defect barriers.

In summary, the 3D AFM topographies provide direct physical evidence that gamma irradiation acts as a dual-regime tool in ZrO_2 -modified $Bi_{0.85}Sb_{0.15}$Te extruded alloys: low-dose exposure (1 Mrad) induces structural relaxation and defect rearrangement that improves matrix homogeneity, whereas high-dose exposure (10–50 Mrad) triggers defect condensation, crystallite size reduction, and surface

fragmentation. These morphological findings fully validate the non-monotonic behavior observed in the cryogenic electrical and thermal transport properties.

To probe the vibrational modes, local chemical bonding, and crystal lattice integrity of Te-doped, ZrO_2-modified $Bi_{0.85}Sb_{0.15}$ extruded composites as a function of gamma radiation dose (0, 1, 10, and 50 Mrad), Raman spectroscopy was performed in the wavenumber range of 200–3700 cm^{-1} (Fig. 5).

Low-Frequency Optical Modes (~480–500 cm^{-1}): The prominent broad vibrational band observed in the lower spectral region corresponds to the characteristic optical lattice vibrations of the rhombohedral Bi - Sb framework coupled with the E_g and A_{1g} vibrational modes of the monoclinic ZrO_2 nanoparticle phase. As the gamma radiation dose increases from 0 Mrad to 50 Mrad, this band undergoes a subtle intensity modification and peak broadening. This broadening directly confirms the radiation-induced generation of localized point defects and the partial breakdown of long-range lattice translational symmetry, consistent with the crystallite size reduction established via XRD.

- Sharp Localized Peak (~1350 cm^{-1}): A well-defined, sharp vibrational feature is identified at approximately 1350 cm^{-1} across the spectra. This sharp peak is associated with localized defect-activated modes and internal elastic micro-strain fields generated at the interface between the $Bi_{0.85}Sb_{0.15}$ matrix and ZrO_2 dispersoid boundaries. The intensity variation of this sharp line across doses highlights the dynamic rearrangement of radiation defects and stress relaxation within the composite lattice.
- High-Frequency Overtone Features (~2400 cm^{-1}): The broad secondary feature centered near 2400 $cm^{-1}$is attributed to multi-phonon higher-order (overtone) scattering processes in the modified semiconductor alloy.

Importantly, no new phase-transformation-related Raman peaks are introduced following gamma irradiation up to 50 Mrad. This structural permanence indicates that exposure to high-energy gamma quanta does not trigger chemical decomposition or secondary phase precipitation within the ZrO_2-modified $Bi_{0.85}Sb_{0.15}$Te matrix. Instead, gamma irradiation selectively modulates the defect concentration and lattice strain state. These Raman spectroscopic findings provide strong complementary evidence to the XRD and 3D AFM data, supporting the mechanism of radiation-controlled defect dynamics and phonon scattering enhancement in these cryogenic materials.

3.2. Temperature-Dependent Electrical and Hall Transport

The temperature dependencies (77–300 K) of electrical conductivity (σ), Seebeck coefficient (α), and Hall coefficient (R_H) for ZrO_2-modified $Bi_{0.85}Sb_{0.15}$Te samples under pristine and irradiated conditions are illustrated in Fig. 4 and Fig. 5.

At cryogenic temperatures (~77 K), the response of transport parameters to radiation dose displays a clear non-monotonic trend:

- Low-dose regime (1 Mrad): Electrical conductivity (σ) increases notably, accompanied by a slight drop in the Seebeck coefficient (α). This behavior is attributed to the radiation-induced introduction of acceptor-type (negatively charged) point defects. These primary defects are generated in the vicinity of positively charged ionic cores, leading to core neutralization and a reduction in charge carrier impurity scattering efficiency—a phenomenon analogous to the "low-dose effect" observed in silicon (Table 2).
- High-dose regime (10–50Mrad): Higher radiation doses lead to an accumulation of radiation defects that capture free carriers. The resulting reduction in free carrier density (n) shifts the Fermi level deeper into the bandgap, decreasing σ while raising the thermoelectric voltage coefficient α and the overall compensation degree [30].

Table 2
Electrical and thermal parameters of extruded samples of solid solution $Bi_{0.85}Sb_{0.15}$Te modified with ZrO_2.

Radiation doses	**Compositions**	**At 77 K**					
		σ, $\Omega^{-1}cm^{-1}$	**α, μV/K**	**χ, Vt/m·K**	**$R_H \cdot 10^{-8}$, cm^3/C**	**μ, $cm^2/V \cdot s$**	**n, cm^{-3}**
0 Mrad	$Bi_{0.85}Sb_{0.15}$	5250	-182	3,02	-26,5	139125	$0,24 \cdot 10^{18}$
	$Bi_{0.85}Sb_{0.15}$+1%ZnO_2	4899	-134	2,93	-14,33	70203	$0,44 \cdot 10^{18}$
	$Bi_{0.85}Sb_{0.15}$Te +1%ZnO_2	6704	-119	3,26	7,9	52962	$0,79 \cdot 10^{18}$
1 Mrad	$Bi_{0.85}Sb_{0.15}$Te +1%ZnO_2	7598	-120	3,87	28,7	218063	$0,22 \cdot 10^{18}$
10Mrad	$Bi_{0.85}Sb_{0.15}$Te +1%ZnO_2	7698	-113	3,37	24,5	188601	$0,26 \cdot 10^{18}$
50 Mrad	$Bi_{0.85}Sb_{0.15}$Te +1%ZnO_2	5937	-121	5,11	33,1	196515	$0,19 \cdot 10^{18}$

The temperature dependence of the Hall coefficient (R_H) weakens significantly in all tellurium-doped, gamma-irradiated specimens compared to pristine samples. The calculated Hall mobility ($\mu_H = \sigma R_H$) across all irradiated composite samples remains substantially higher than in unirradiated modified alloys (Table 2). However, beyond 1 Mrad, carrier mobility decreases monotonically with increasing radiation dose (with a localized anomaly at 10 Mrad). Tellurium doping enhances electrical conductivity relative to undoped alloys by supplying donor charge carriers, though carrier mobility decreases with temperature across the entire range (77–300 K) due to intensified lattice phonon scattering.

3.3. Thermal Conductivity Deconvolution and Phonon Dynamics

The measured total thermal conductivity (χ) increases monotonically with temperature for all investigated alloys. Gamma irradiation elevates χ across the entire temperature interval relative to pristine specimens (with the exception of the 1 Mrad sample). At low temperatures (~77 K), thermal energy in the $Bi_{0.85}Sb_{0.15}$ matrix is transported predominantly by acoustic lattice phonons and conduction electrons [33–35]. To isolate these mechanisms, the total thermal conductivity was deconvoluted into electronic (χ_e) and lattice (χ_l) components using the expressions:

$$\chi = \chi_e + \chi_l \quad (1)$$

$$\chi_e = L \sigma T \quad (2)$$

where $L = A (k/e)^2$ is the Lorentz number, k is the Boltzmann constant, e is the elementary charge, and the parameter A was evaluated from the experimental Seebeck coefficient according to [36].

The calculated electronic component χ_e at ~77 K for pristine, 1 Mrad, 10 Mrad, and 50 Mrad irradiated modified samples yields 0.92, 1.00, 1.10, and 0.80 W/m·K, respectively. The corresponding lattice thermal conductivities (χ_l) are 2.34, 2.87, 2.27, and 4.31 W/m·K. These results confirm that lattice vibrations carry the dominant fraction of heat at 77 K (~ 72% in pristine samples; ~74%, ~67%, and ~85% in 1, 10, and 50 Mrad irradiated samples, respectively). The high-dose enhancement of total thermal conductivity (χ) is primarily governed by an increase in the lattice component (χ_l), driven by structural point defect rearrangements and strain field homogenization within individual extruded grains.

3.4. Magnetoelectric Response and Scattering Mechanisms

The magnetic field dependencies of electrical conductivity σ(H) and Seebeck coefficient α(H) under transverse magnetic fields up to H = 740 kA/m at ~77 K are presented in Fig. 6.

Applying a transverse magnetic field deflects moving electrons and holes via the Lorentz force, altering the relative contributions of high-mobility and low-mobility carriers to the total current. In weak magnetic fields (up to ~160 kA/m), the transverse magnetoresistance ($\Delta\rho/\rho_0$) of unirradiated alloys is substantially higher than that of irradiated samples. At higher field strengths, the magnetic response converges across all specimens as defect scattering dominates over phonon scattering.

The transverse magnetoresistance in the weak-field regime follows the classic quadratic relation [37]:

$$\Delta\rho/\rho_0 = A \mu^2 B^2 \quad (3)$$

where B is the magnetic induction and A is a dimensionless factor dependent on the dominant carrier scattering mechanism. Experimental $\Delta\rho/\rho_0$ data plotted against B^2 yield excellent agreement with a value of A = 1.18, confirming predominantly isotropic electron scattering in ZrO_2-modified $Bi_{0.85}Sb_{0.15}$. Because the density of deformation-induced structural defects in pristine samples is low at ~77 K, acoustic phonon scattering dominates, yielding a sharp increase in the Seebeck coefficient (α) under an applied magnetic field. In irradiated samples, the interaction between radiation-induced point defects and deformation-induced dislocation networks reduces internal lattice micro-strains, facilitating a radiation-stimulated enhancement in carrier mobility and stabilizing magnetoelectric response across cryogenic temperatures.

4. Conclusion

In this study, the structural, micro-morphological, vibrational, and low-temperature (77–300 K) transport properties of hot-extruded $Bi_{0.85}Sb_{0.15}$Te alloys modified with 1 wt %, ZrO_2 were systematically investigated under gamma irradiation (1–50 Mrad). The main findings are summarized as follows:

- Structural Integrity and Phonon Dynamics: XRD refinement confirmed crystallite size reduction and peak broadening without fundamental lattice parameter changes. Raman spectra verified phase stability up to 50 Mrad, with low-frequency mode broadening (~ 480–500 cm^{-1}) and a sharp strain peak (~1350 cm^{-1}) reflecting radiation defect generation and micro-strain redistribution.
- Micro-Morphological Evolution: 3D AFM topographies demonstrated a dual-regime mechanism: low doses (1Mrad) induce micro-stress relaxation and surface smoothing via point defect migration, whereas high doses (10–50 Mrad) trigger defect condensation, ridge formation, and crystallite fragmentation.
- Transport Anomalies and Low-Dose Effect: In ZrO_2-modified samples, low-dose (Mrad) irradiation introduces acceptor-type centers that partially neutralize positive ionic cores. This suppresses impurity scattering and yields a radiation-stimulated enhancement in carrier mobility (μ_H). At higher doses, carrier trapping at radiation levels decreases conductivity (σ).
- Thermal Transport: Thermal conductivity deconvolution at 77 K confirmed that heat transport is lattice-dominated (~ 67–85). The increase in total thermal conductivity at high doses is driven by χ_l enhancement due to defect rearrangement.

In summary, controlled gamma irradiation combined with ZrO_2 dispersion serves as an effective mechanism for defect engineering and transport optimization in cryogenic Bi - Sb thermoelectric materials.

Declarations

Competing Interests

The authors have no relevant financial or non-financial interests to disclose. No potential conflict of interest was reported by the author(s).

Funding

The topic of the article is related to the budget-funded research work of the Institute of Physics, Ministry of Science and Education of the Republic of Azerbaijan (Project years: 2025–2028). The results of the research presented in the manuscript were obtained on the basis of experiments conducted at the Institute of Physics of the Ministry of Science and Education of Azerbaijan.

Author Contribution

I.A. Abdullayeva: Conceptualization, Methodology, Formal analysis, Investigation, Data curation, Writing – original draft, Visualization, Project administration. B.Q. Mehdiyev: Conceptualization, Methodology, Validation, Resources, Writing – review & editing, Supervision. All authors critically reviewed and revised the manuscript for important intellectual content, gave their final approval of the version to be published, and agreed to be accountable for all aspects of the work.

Data Availability

All data generated or analyzed during this study are included in this published article.

References

1. V.S. Zemskov, A.D. Belaya, S.A. Roslov et al., Izv. Akad. Nauk. SSSR Met. **1**, 73 (1978)
2. L.A. Belozerova, Kholodiln Tekh. Tekhnol. **23**, 52 (1976)
3. D.Z. Grabko, Y.S. Boyarskaya, M.P. Dyntu, *Mechanical Properties of Bismuth-Type Semimetals* (Shtiintsa, Chisinau, 1982), p. 136
4. M.P. Banaga, O.B. Sokolov, T.E. Benderskaya, L.D. Dudkin, A.B. Ivanova, I.I. Fridman, Izv. Akad. Nauk. SSSR Neorg Mater. **22**(4), 619 (1986)
5. M.M. Tagiev, Z.F. Agaev, D.S. Abdinov, Inorg. Mater. **30**(3), 375 (1994)
6. M.M. Tagiev, Inorg. Mater. **57**(2), 119 (2021). https://doi.org/10.1134/S0020168521020150
7. M.M. Tagiyev, S.Z. Jafarova, A.M. Akhmedova, G.D. Abdinova, Russ Phys. J. **62**(3), 510 (2019). https://doi.org/10.1007/s11182-019-01740-9
8. I.A. Abdullaeva, G.D. Abdinova, M.M. Tagiyev, B.S. Barkhalov, Inorg. Mater. **57**(9), 887 (2021). https://doi.org/10.1134/S0020168521090015
9. M. Paulescu, D. Vizman, M. Lascu, R. Negrila, M. Stef, AIP Conf. Proc. 1796(1), 020002 (2017). https://doi.org/10.1063/1.4972388

10. S. Park, J.C. Bourgoin, H. Sim, C. Baur, V. Khorenko, O. Cavani, J. Bouquerel, S. Picard, B. Boizot, Prog Photovolt. Res. Appl. **26**(10), 778 (2018). https://doi.org/10.1002/pip.3016
11. I.A. Abdullayeva, G.D. Abdinova, M.M. Tagiyev, O.A. Samedov, Int. J. Mod. Phys. B **35**(07), 2150099 (2021). https://doi.org/10.1142/S0217979221500995
12. O.A. Oraby, M.F. El-Kordy, H.T. El-Madany, F.H. Fahmy, Int. J. Sci. Eng. Technol. Res. **3**(2), 167 (2014)
13. I. Mili, H. Latelli, T. Ghellab, Z. Charifı, H. Baaziz, F. Soyalp, Int. J. Mod. Phys. B **35**(07), 2150100 (2021). https://doi.org/10.1142/S0217979221501009
14. Y. Zhou, Z. Ge, J. Guo, J. Feng, Mod. Phys. Lett. B **34**(18), 2050206 (2020). https://doi.org/10.1142/S0217984920502061
15. C. Wu, B. Sun, Z. Wang, J. Liu, Z. Pang, Y. Li, L. Cao, Y. Yang, X. Liu, J. Zhao, H. Ma, Mod. Phys. Lett. B **34**(31), 2050357 (2020). https://doi.org/10.1142/S0217984920503571
16. M. Tan, W.D. Liu, X.L. Shi, J. Shang, Z.G. Chen, Adv. Energy Mater. **11**(40), 2102578 (2021). https://doi.org/10.1002/aenm.202102578
17. Y. Wang, L. Zhang, Q. Lu, C. Liu, W. Liu, Z.G. Chen, Chem. Eng. J. **397**, 125360 (2020). https://doi.org/10.1016/j.cej.2020.125360
18. Y. Wang, M.H. Liu, W.D. Liu, X.L. Shi, S.D. Xu, Q. Sun, H. Gao, S. Lu, J. Zou, Z.G. Chen, Nano Energy. **78**, 105379 (2020). https://doi.org/10.1016/j.nanoen.2020.105379
19. L.D. Ivanova, Semiconductors. **51**(7), 909 (2017). https://doi.org/10.1134/S1063782617070132
20. K.I. Portnoy, B.N. Babich, *Dispersion-Strengthened Materials* (Metallurgiya, Moscow, 1974), p. 199
21. M.G. Dick, D.S. Abdinov, Izv. Akad. Nauk. SSSR Neorg Mater. **24**(8), 1290 (1988)
22. L.I. Zadvorny, Y.M. Goryachev, *Abstracts of All-Union Seminar on Semiconductor Materials for Thermoelectric Converters* (LPTI, Leningrad, 1985), pp. 108–109
23. A.G. Volkov, N.A. Dyugaeva, G.N. Kuvyrkin et al., Cosm. Res. **55**, 124 (2017). https://doi.org/10.1134/S0010952517020071
24. J.H. Lehman, B. Lee, E.N. Grossman, Appl. Opt. **50**(21), 4099 (2011). https://doi.org/10.1364/AO.50.004099
25. N.A. Sidorenko, Z.M. Dashevsky, Semiconductors. **53**(5), 686 (2019). https://doi.org/10.1134/S1063782619050245
26. D.M. Heiker, L.S. Zevin, *X-Ray Diffractometry* (Fizmatgiz, Moscow, 1963), p. 380
27. A.K. Pikaev, *Dosimetry in Radiation Chemistry* (Nauka, Moscow, 1975), p. 232
28. T.D. Alieva, D.S. Abdinov, E.Y. Salaev, Izv. Akad. Nauk. SSSR Neorg Mater. **17**(10), 1773 (1981)
29. A.S. Okhotin, A.S. Pushkarsky, R.P. Borovikova, V.A. Smirnov, *Methods for Measuring Characteristics of Thermoelectric Materials and Converters* (Nauka, Moscow, 1974), p. 168
30. G.P. Gaidar, Semiconductors. **48**(9), 1147 (2014). https://doi.org/10.1134/S1063782614090097
31. V.S. Zemskov, A.D. Belaya, *Study of Growth Conditions of Single Crystals on Structure and Properties of Bismuth-Antimony Alloys* (VINITI, Baikov Institute of Metallurgy, Moscow, 1981), p. 20

32. A.N. Dubrovina, L.A. Leonteva, G.A. Drozdova et al., Inorg. Mater. **17**(4), 613 (1981)
33. V.S. Zemskov, P.G. Borodin, A.D. Belaya, S.A. Roslov, *Transport Phenomena in Bismuth and Bismuth-Antimony Solid Solutions* (VINITI, Baikov Institute of Metallurgy, Moscow, 1978), p. 52
34. M.M. Tagiev, Z.F. Agaev, D.S. Abdinov, Inorg. Mater. **30**(6), 776 (1994)
35. Z.F. Agaev, G.D. Abdinova, G.Z. Bagieva, M.M. Tagiev, D.S. Abdinov, Inorg. Mater. **44**(2), 97 (2008). https://doi.org/10.1134/S0020168508020027
36. V.S. Oskotsky, I.A. Smirnov, *Defects in Crystals and Thermal Conductivity* (Nauka, Leningrad, 1972), p. 160
37. A.F. Ioffe, *Semiconductor Thermoelements* (Nauka, Moscow-Leningrad, 1960), p. 186

Figures

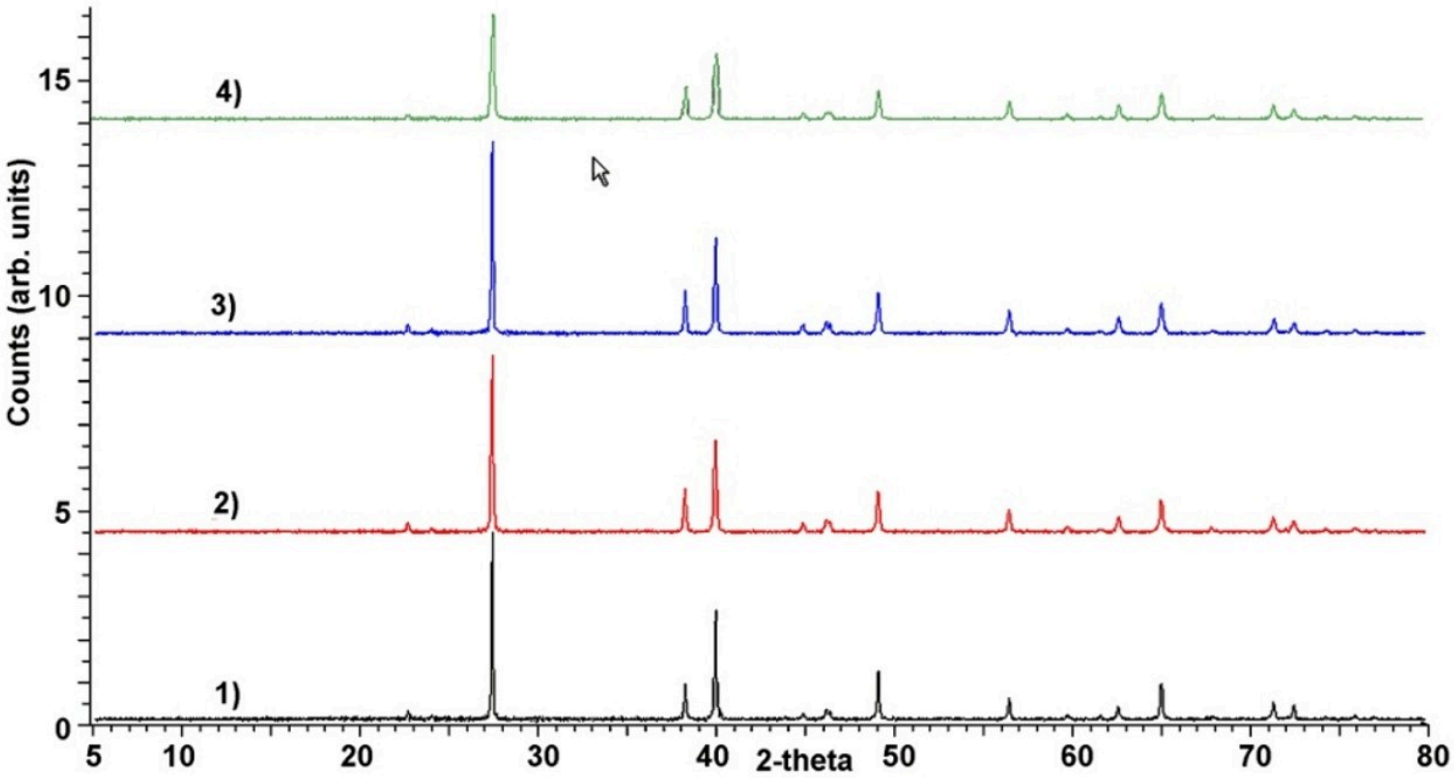


Figure 1

Diffraction spectra of $Bi_{0.85}Sb_{0.15}$□Te□ modified ZrO_2 before and after irradiation: 1) without irradiation, 2, 3, 4) 1, 10, 50 Mrad, respectively.

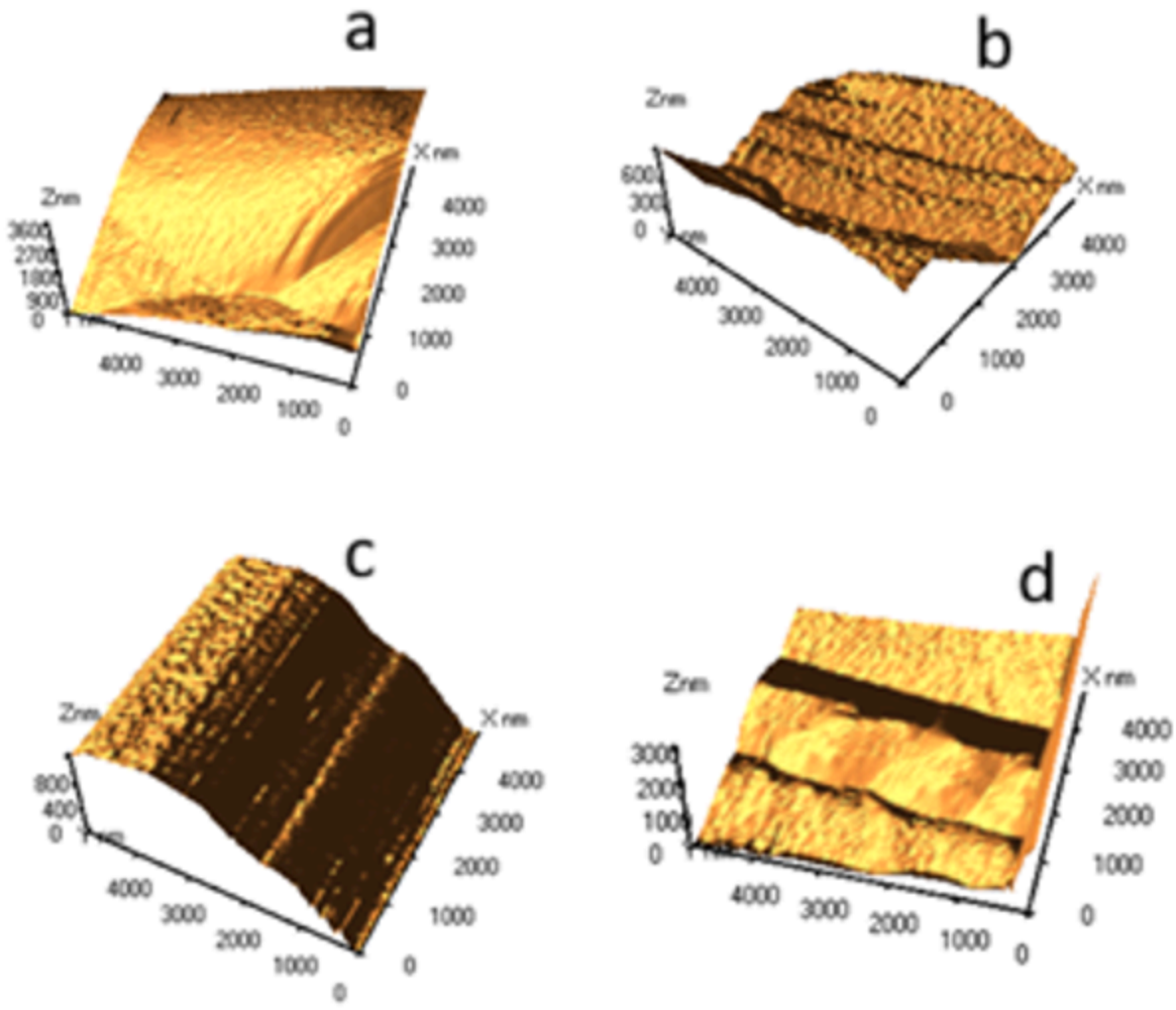


Figure 2

3D AFM surface topographies of ZrO_2-modified $Bi_{0.85}Sb_{0.15}$Te extruded samples: (**a**) pristine (unirradiated), and irradiated with gamma quanta at doses of (**b**) 1 Mrad, (**c**) 10 Mrad, and (**d**) 50 Mrad.

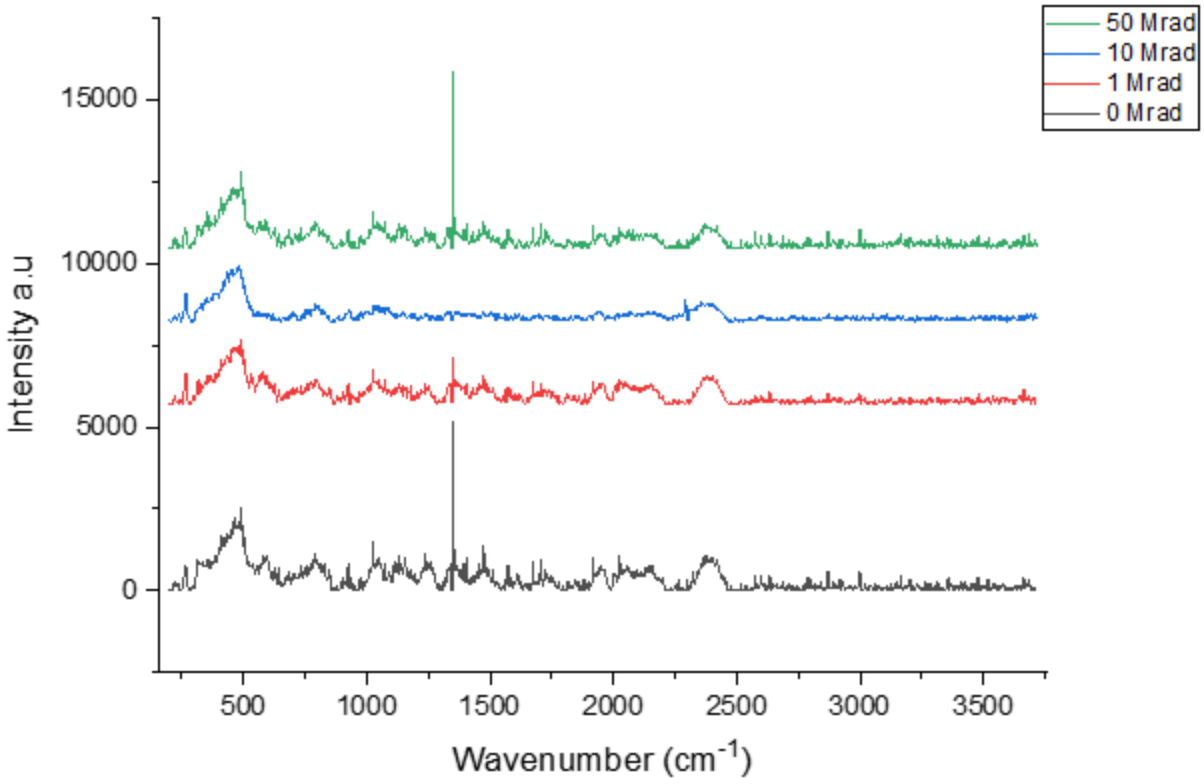


Figure 3

Raman spectra of ZrO_2-modified $Bi_{0.85}Sb_{0.15}$Te extruded samples in the pristine state (0 Mrad, black curve) and after gamma-quanta irradiation at doses of 1 Mrad (red curve), 10 Mrad (blue curve), and 50 Mrad (green curve).

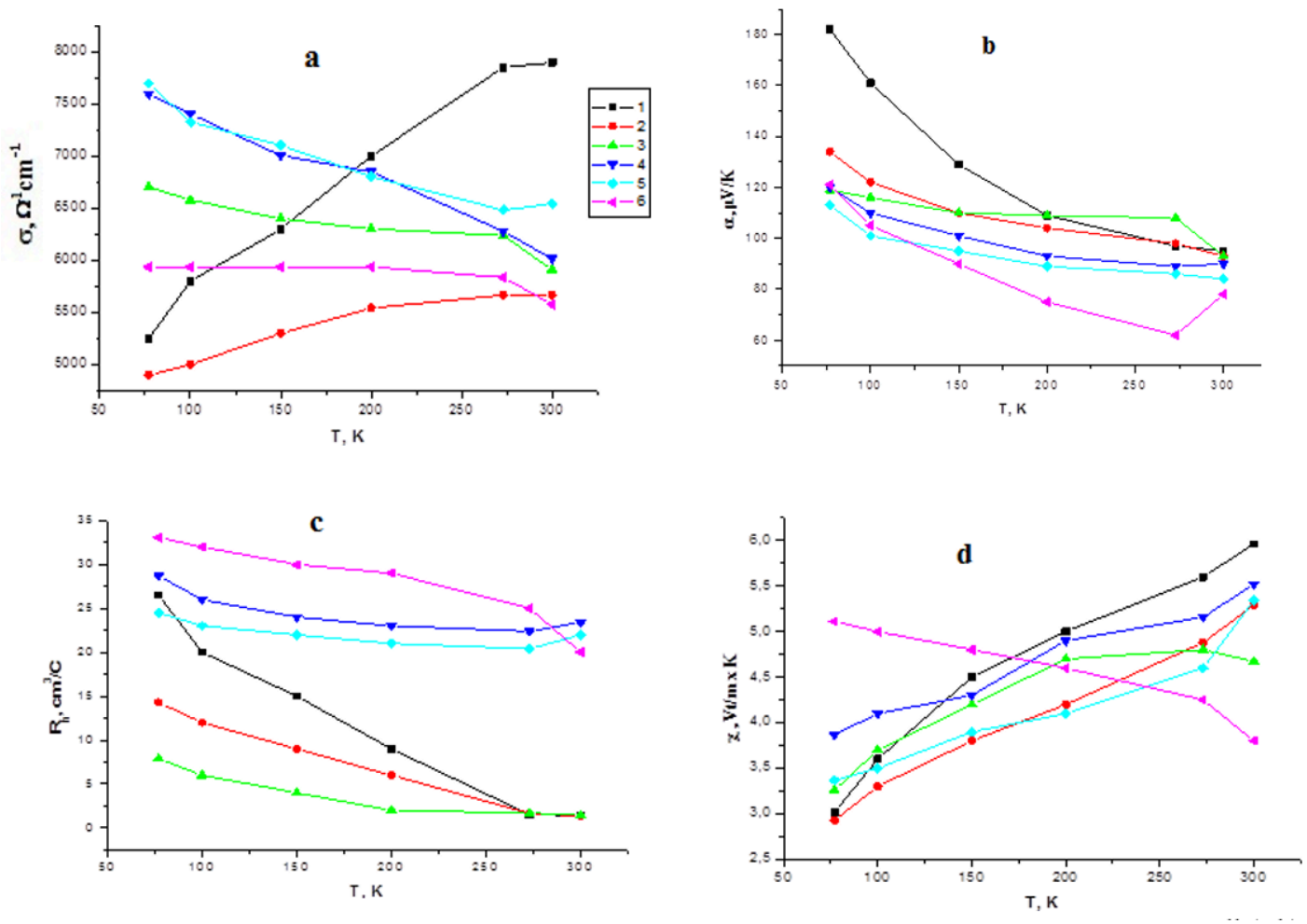


Figure 4

Temperature dependences of electrical conductivity (a), thermoelectric power coefficients α (b), Hall (Rh) and thermal conductivity χ (d) of extruded samples of $Bi_{0.85}Sb_{0.15}$Te solid solution modified with ZrO_2. 1- $Bi_{0.85}Sb_{0.15}$ unmodified and unirradiated sample; 2- $Bi_{0.85}Sb_{0.15}$+ 1% ZnO_2 unirradiated; 3- $Bi_{0.85}Sb_{0.15}$<Te> modified ZrO_2; 4-6 samples of $Bi_{0.85}Sb_{0.15}$ <Te> modified ZrO_2 irradiated with gamma quanta of 1 Mrad, 10 Mrad and 50 Mrad, respectively.

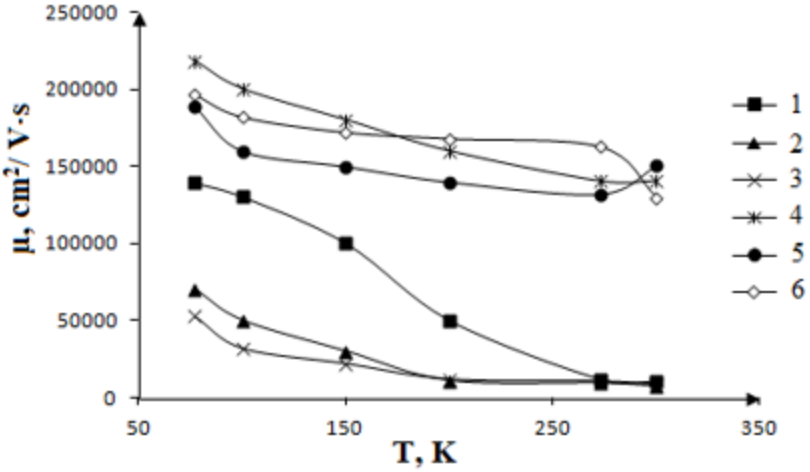


Figure 5

Temperature dependences of mobility (μ) of extruded samples of solid solution $Bi_{0.85}Sb_{0.15}$Te modified with ZrO_2. The designations are the same as in Fig. 4.

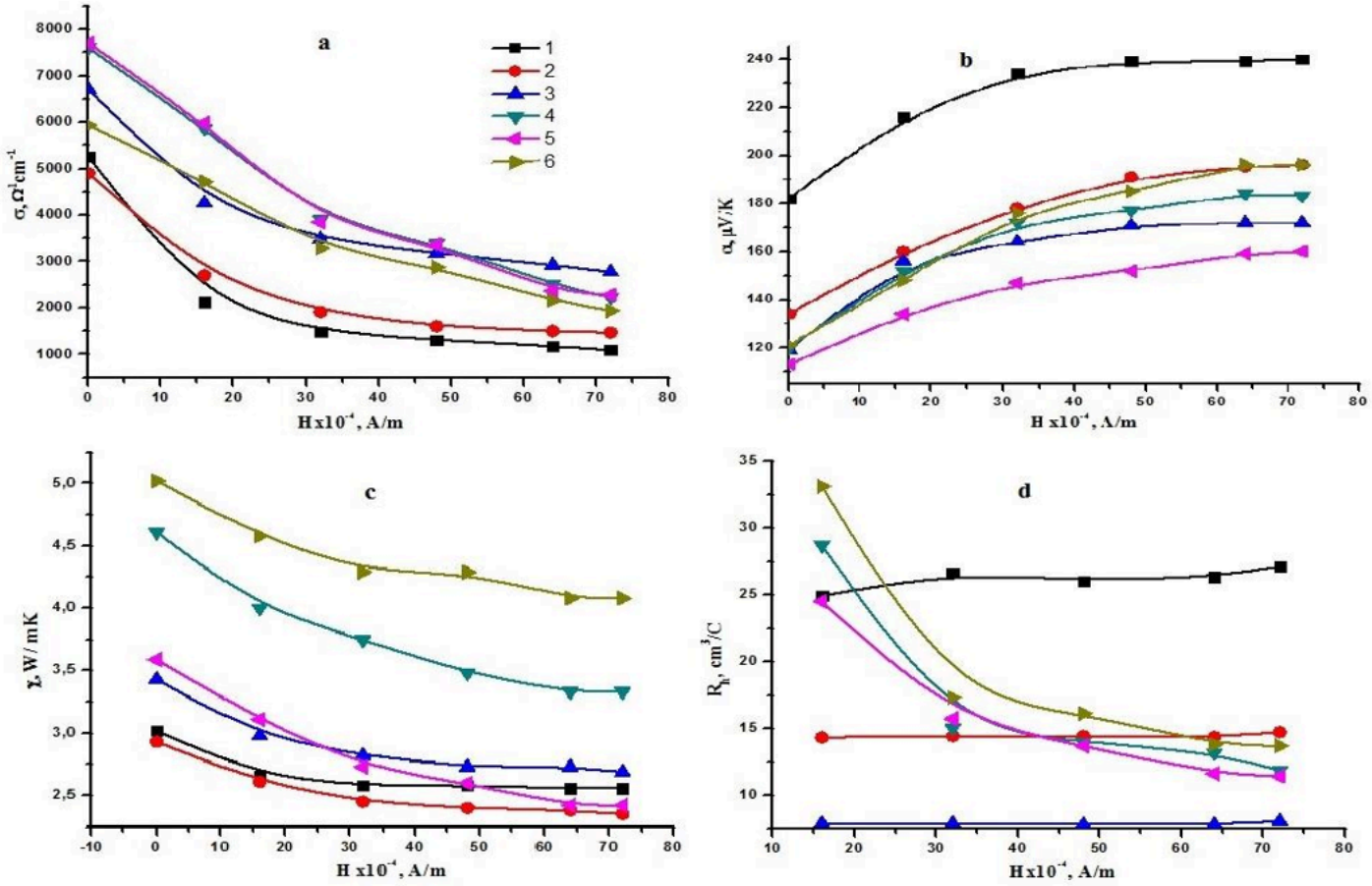


Figure 6

Dependences of electrical conductivity (a), thermoelectric coefficients α (b), Hall (R_H) and thermal conductivity χ (d) on the magnetic field strength (H) of extruded samples of $Bi_{0.85}Sb_{0.15}$Te solid solution modified with ZrO_2 at ~ 77K. The designations are the same as in Fig. 4.